

RESEARCH LETTER

10.1002/2016GL069877

Special Section:

First results from NASA's Magnetospheric Multiscale (MMS) Mission

Key Points:

- High-resolution observations of cold ions near the X-line
- Cold ions decouple from hot ions inside the separatrix and follow the electron motion
- A layer at cold ion scales (cold IDR) is found near the X-line where cold ions are demagnetized and accelerated parallel to E

Supporting Information:

- Supporting Information S1
- Figure S1
- Figure S2

Correspondence to:

S. Toledo-Redondo, sergiotr@ugr.es

Citation:

Toledo-Redondo, S., et al. (2016), Cold ion demagnetization near the X-line of magnetic reconnection, *Geophys. Res. Lett.*, 43, 6759–6767, doi:10.1002/2016GL069877.

Received 1 APR 2016

Accepted 20 JUN 2016

Accepted article online 27 JUN 2016

Published online 13 JUL 2016

Cold ion demagnetization near the X-line of magnetic reconnection

Sergio Toledo-Redondo¹, Mats André², Yuri V. Khotyaintsev², Andris Vaivads², Andrew Walsh¹, Wenya Li², Daniel B. Graham², Benoit Lavraud^{3,4}, Arnaud Masson¹, Nicolas Aunai⁵, Andrey Divin^{2,6}, Jeremy Dargent^{3,4,5}, Stephen Fuselier^{7,8}, Daniel J. Gershman⁹, John Dorelli⁹, Barbara Giles⁹, Levon Avakov^{9,10}, Craig Pollock⁹, Yoshifumi Saito¹¹, Thomas E. Moore⁹, Victoria Coffey¹², Michael O. Chandler¹², Per-Arne Lindqvist¹³, Roy Torbert¹⁴, and Christopher T. Russell¹⁵

¹Science Directorate, European Space Agency, ESAC, Madrid, Spain, ²Swedish Institute of Space Physics, Uppsala, Sweden, ³Institut de Recherche en Astrophysique et Planétologie, Université de Toulouse (UPS), Toulouse, France, ⁴Centre National de la Recherche Scientifique, Toulouse, France, ⁵Laboratory of Plasma Physics-École Polytechnique, CNRS, UPMC, Université Paris-Sud, Paris, France, ⁶Faculty of Physics, Earth Physics Department, Saint Petersburg State University, Saint Petersburg, Russia, ⁷Southwest Research Institute, San Antonio, Texas, USA, ⁸Space Science Department, University of Texas at San Antonio, San Antonio, Texas, USA, ⁹NASA Goddard Space Flight Center, Greenbelt, Maryland, USA, ¹⁰Department of Astronomy, University of Maryland, College Park, Maryland, USA, ¹¹Institute for Space and Astronautical Science, Sagami-hara, Japan, ¹²NASA Marshall Space Flight Center, Huntsville, Alabama, USA, ¹³Department of Space and Plasma Physics, Royal Institute of Technology, Stockholm, Sweden, ¹⁴Institute for the Study of Earth, Oceans, and Space, University of New Hampshire, Durham, New Hampshire, USA, ¹⁵Department of Earth and Space Sciences, University of California, Los Angeles, California, USA

Abstract Although the effects of magnetic reconnection in magnetospheres can be observed at planetary scales, reconnection is initiated at electron scales in a plasma. Surrounding the electron diffusion region, there is an Ion-Decoupling Region (IDR) of the size of the ion length scales (inertial length and gyroradius). Reconnection at the Earth's magnetopause often includes cold magnetospheric (few tens of eV), hot magnetospheric (10 keV), and magnetosheath (1 keV) ions, with different gyroradius length scales. We report observations of a subregion inside the IDR of the size of the cold ion population gyroradius (~15 km) where the cold ions are demagnetized and accelerated parallel to the Hall electric field. Outside the subregion, cold ions follow the $\mathbf{E} \times \mathbf{B}$ motion together with electrons, while hot ions are demagnetized. We observe a sharp cold ion density gradient separating the two regions, which we identify as the cold and hot IDRs.

1. Introduction

Magnetic reconnection is a process that connects previously separated plasma regimes, permitting them to exchange mass and energy, while converting large amounts of magnetic energy into kinetic energy. Its effects can be observed at the largest scales of the system (e.g., magnetospheres), although it initiates at the electron scales of the plasma. At these scales, in the so-called Electron Diffusion Region (EDR), the plasma is believed to become diffusive and magnetic field lines reconfigure, changing their magnetic field topology [Burch et al., 2016].

Due to their larger mass, the ion characteristic length scale (i.e., inertial length and gyroradius) is larger than that of electrons. Below the ion scale, ions decouple from electrons and the Magnetohydrodynamics formalism is no longer valid. A two-fluid description is then more appropriate to describe their dynamics. From the stationary electron momentum equation, neglecting the inertial term, one can derive the generalized Ohm's law:

$$\mathbf{E} + \mathbf{v}_i \times \mathbf{B} = \frac{1}{en} \mathbf{j} \times \mathbf{B} - \frac{1}{en} \nabla \cdot \mathbf{P}_e, \quad (1)$$

where \mathbf{E} and \mathbf{B} correspond to the electric and magnetic fields, \mathbf{v}_i to the ion bulk velocity, \mathbf{j} to the current, n to the number density, e to the electron charge, and \mathbf{P}_e the electron pressure. The left-hand side of the equation corresponds to the ion frozen-in condition. The terms on the right-hand side account for the two-fluid effects, and they are important inside structures smaller than the ion length scale.

When reconnection occurs, the frozen-in condition is broken in several regions: inside the EDR, around the EDR in a region commonly named Ion-Decoupling Region (IDR), in the separatrices, or inside the exhausts [e.g., Pritchett, 2008]. In these regions, owing to the decoupled ion and electron motions, large currents are set up, together with Hall magnetic fields [Pritchett and Mozer, 2009].

Cold ions (up to few tens of eV) often reach the dayside magnetopause [e.g., Sauvaud et al., 2001; André and Cully, 2012; Lee et al., 2016; Chandler and Moore, 2003; Chen and Moore, 2006] and participate in reconnection [e.g., Chandler et al., 1999; Chen and Moore, 2004]. They belong to the plasma cloak, plasmaspheric wind, or plasmaspheric drainage plumes [e.g., Chappell et al., 2008; Darrouzet et al., 2008]. They can be very dense and usually contain heavy ions [Darrouzet et al., 2009]. Therefore, they mass load the plasma and the associated Alfvén velocity and reconnection rate are reduced [Cassak and Shay, 2007; Borovsky et al., 2008; Walsh et al., 2013, 2014; Wang et al., 2015; Fuselier et al., 2016].

In addition to the mass-loading effect, the magnetospheric cold ion gyroradius is about 1 order of magnitude smaller than that of the magnetospheric hot ions. Consequently, the cold population can remain magnetized inside structures of size comparable to the hot ion gyroradius [André et al., 2010], reducing the Hall currents carried by electrons, as observed in the separatrices of magnetic reconnection [Toledo-Redondo et al., 2015].

In this work, we present observations with unprecedented resolution made by the Magnetospheric Multiscale (MMS) mission [Burch et al., 2015] of the IDR of magnetic reconnection in the subsolar magnetopause under the presence of cold ions. We can resolve, for the first time, physics occurring at the cold ion length scale. Close to the X-line, inside the IDR, we identify a subregion of large Hall \mathbf{E} field (30 mV/m, normal to the magnetopause) and size comparable to the cold ion gyroradius (~ 15 km) where the cold ions are demagnetized and accelerated parallel to \mathbf{E} , as opposed to the observations in the separatrix and the IDR where the cold ions follow $\mathbf{E} \times \mathbf{B}$ motion. The MMS tetrahedron configuration allowed us to identify a sharp cold ion density gradient separating the two regions: the hot and cold IDRs. This work presents evidence of a multilayered IDR owing to the presence of ion populations with different temperature.

2. Event Overview

The MMS mission is composed of four spacecraft, equipped with an identical suite of plasma instrumentation. The mission was launched in March 2015 with the aim of studying the microphysics of magnetic reconnection. Owing to their high-resolution measurements in conjunction with an interspacecraft separation of the order of 10 km, the smallest kinetic scales of magnetic reconnection can be resolved, including electron and cold ion scales, for the first time.

On 22 October 2015 at around 06:05 UTC, MMS crossed the dayside magnetopause at [9.63, 3.98, -0.32] R_E (Earth radii) in Geocentric Solar Ecliptic (GSE) coordinates (Figure 1a). Figure 1b shows the asymmetric reconnection topology in a particle-in-cell simulation, where the normal electric field (E_n) is color coded. Details of the simulation can be found in the supporting information of Lavraud et al. [2016]. The approximate trajectory of MMS is plotted on top. The first crossing, label 1, corresponds to a separatrix crossing from the magnetosphere into the southward jet. Between the two jets, i.e., in the region between the labels 2 and 3, there is another region where a mixture of magnetospheric and magnetosheath populations can be found. Inside this region, ions are decoupled from the electron motion, as we discuss later.

The four spacecraft are in a tetrahedron configuration with average separation ~ 15 km (Figure 1c). Figures 1d–1h correspond to MMS4 observations. MMS1–3 show nearly identical measurements at the time scale of this plot (1 min). During the crossing, the interplanetary magnetic field was southward, and the crossing is seen by MMS as a rotation of B_z , recorded by the Flux Gate Magnetometer (FGM) [Russell et al., 2016] (Figure 1d). The Fast Plasma Instrument (FPI) [Pollock et al., 2016] measures the 3-D ion and electron distribution functions at 150 ms and 30 ms cadence, respectively. The electron and ion number densities (n_i , n_e) observed by FPI are plotted in Figure 1e. The sheath and exhaust densities fluctuate between 15 and 25 cm^{-3} . In the magnetosphere, the presence of cold ions (Figure 1g) and electrons (Figure 1h) makes it difficult to measure the total density. The spacecraft potential (V_{sc}) prevents cold ions from reaching the detector. In addition, cold electrons may be difficult to separate from photoelectrons. V_{sc} remained low during the entire interval of Figure 1 ($V_{sc} < 8$ V). By comparing Figures 1e and 1g, it is concluded that a hidden cold ion population was present during the interval 06:04:50 UTC–06:05:00 UTC. For that interval, n_e is a more reliable measure of the total plasma density, 4–5 cm^{-3} , where ~ 0.4 cm^{-3} corresponds to hot ions and the rest to cold ions.

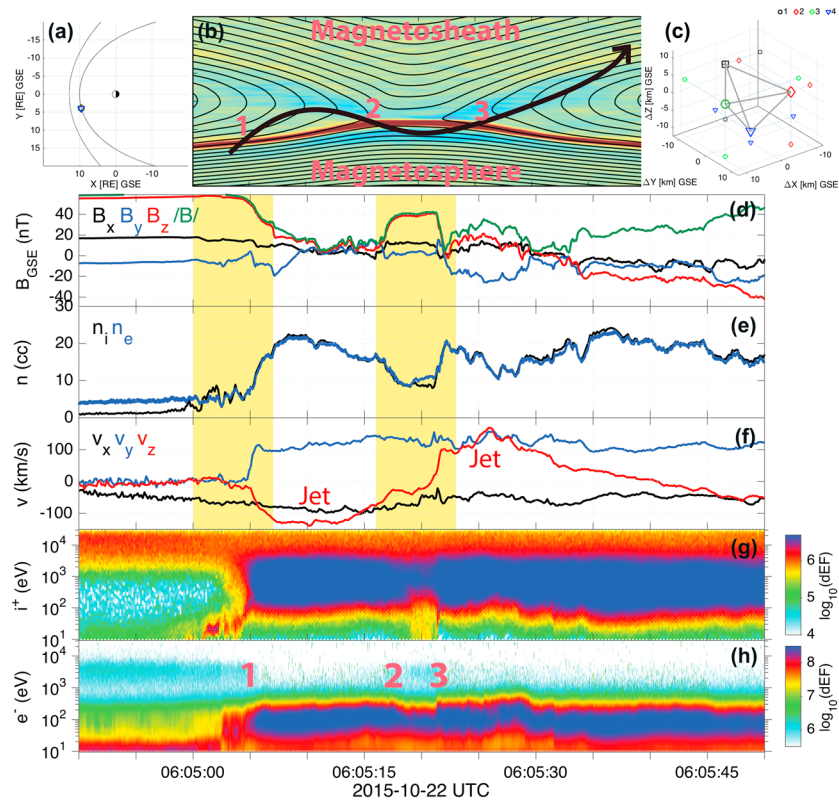


Figure 1. Overview of the 22 October 2015–06:05 UTC magnetopause crossing (MMS4). (a) Spacecraft position in the ecliptic plane. (b) 2D-PIC simulation of asymmetric reconnection. The normal (Hall) electric field is color coded. The approximate trajectory of MMS is plotted on top. (c) Tetrahedron configuration of the MMS spacecraft (~15 km separation). (d) Magnetic field in GSE coordinates. (e) Ion (black) and electron (blue) number densities. (f) Bulk velocity of the plasma in GSE coordinates. (g) Ion differential energy flux in $\text{keV cm}^{-2} \text{s}^{-1} \text{keV}^{-1}$. (h) Electron differential energy flux in $\text{keV cm}^{-2} \text{s}^{-1} \text{keV}^{-1}$.

At 06:05:02 UTC the cold ions become visible to FPI (due to larger $\mathbf{E} \times \mathbf{B}$ motion) and the two density estimations then roughly agree. In Figure 1f, the bulk ion velocity measured by FPI is shown in GSE coordinates. Two jets can be observed during the interval; the first is oriented along $-\mathbf{Z}$ and the second along $+\mathbf{Z}$, with velocities of the order of 150 km/s. This value is roughly consistent with the hybrid Alfvén velocity introduced by Cassak and Shay [2007] for asymmetric reconnection (157 km/s taking $B_{ms} = 50 \text{ nT}$, $B_{sh} = 20 \text{ nT}$, $n_{ms} = 5 \text{ cm}^{-3}$, and $n_{sh} = 25 \text{ cm}^{-3}$). In addition, the magnetosheath ions show $+\mathbf{Y}$ and $-\mathbf{X}$ velocity components, ~ 100 and -50 km/s , respectively, consistent with the expected magnetosheath flow at the spacecraft location (Figure 1a). By looking at the omnidirectional ion differential Energy Flux (dEF) distributions (Figure 1g) measured by FPI, the three ion populations can be distinguished: sheath ions ($\sim 1 \text{ keV}$), magnetospheric cold (below 100 eV) and magnetospheric hot ($\sim 10 \text{ keV}$) ions. Figure 1h shows the omnidirectional electron differential energy flux. On the magnetospheric side a cold electron population can be observed (below 25 eV). They are well above the spacecraft potential ($V_{sc} < 8 \text{ V}$) so it is unlikely that they correspond to spacecraft photoelectrons. Magnetospheric hot electrons can be observed with energies $\sim 3 \text{ keV}$, and the sheath electrons have $\sim 100 \text{ eV}$ energy. The electron edge (i.e., first observation of sheath electron population) indicating the first reconnected line crossing observed at 06:05:02 UTC.

3. Generalized Ohm’s Law Inside the Ion-Decoupling Regions

In this section, we compare the observations of the first separatrix crossing (06:05:02 UTC–06:05:06 UTC) and the IDR near the X-line (06:05:16 UTC–06:05:22 UTC). We estimate the Ohm’s law terms and find that they balance each other within an error of less than 2 mV/m.

Figure 2 shows a summary of MMS4 observations of the first separatrix crossing (06:05:00 UTC–06:05:07 UTC), marked in yellow in Figure 1. Initially, MMS4 is in the magnetosphere and crosses into the southward jet.

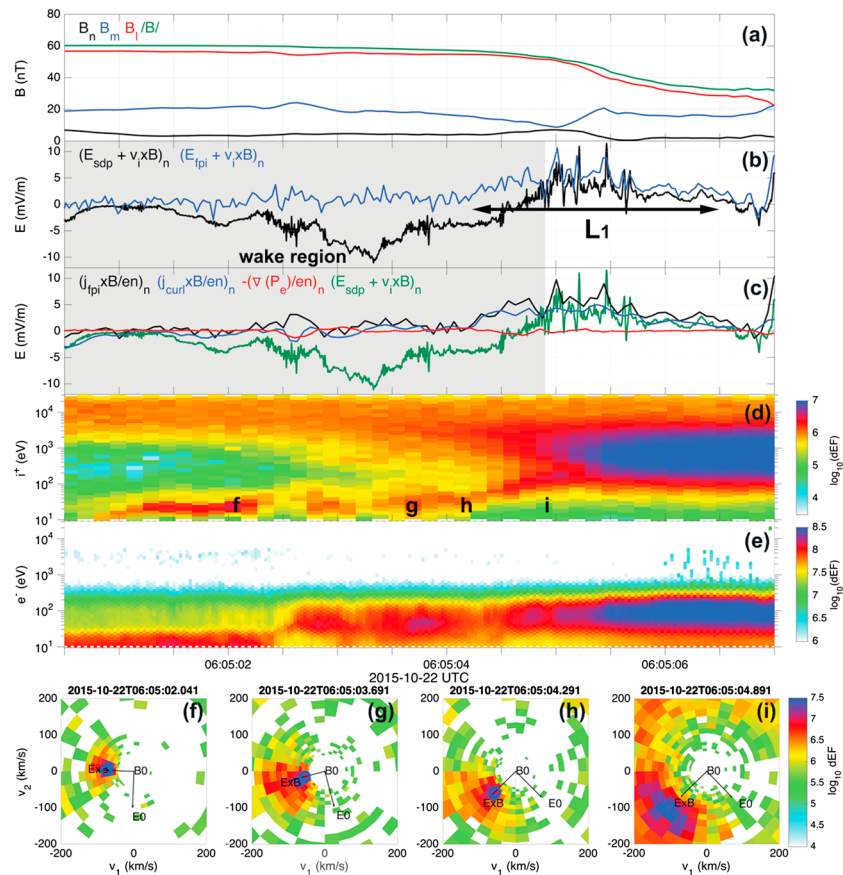


Figure 2. Detail of MMS4 separatrix crossing. (a) Magnetic field in LMN coordinates. (b) \mathbf{N} component of the left-hand side terms of equation (1). \mathbf{E} field is obtained from SDP (E_{sdp} , black) and from electron motion assuming $\mathbf{E} = -\mathbf{v}_e \times \mathbf{B}$ (E_{fpi} , blue). (c) \mathbf{N} component of the right-hand side terms of equation (1). The current is obtained from FPI (\mathbf{j}_{fpi} , black) and from curlometer (\mathbf{j}_{curl} , blue). The estimation of left-hand side terms (\mathbf{N} component) of equation (1) is plotted in green for comparison. (d) Ion differential energy flux in $\text{keV cm}^{-2} \text{s}^{-1} \text{sr}^{-1} \text{keV}^{-1}$. (e) Electron differential energy flux in the perpendicular plane at different times during the crossing. The parameter v_1 is closest to \mathbf{N} and v_2 is roughly $-\mathbf{M}$. The electron bulk velocity is plotted using blue circles. \mathbf{B}_0 is the average magnetic field for the FPI interval (150 ms), obtained from FGM. The \mathbf{E}_0 direction is obtained from the average electron bulk velocity in the interval (150 ms) assuming $\mathbf{E}_0 = -\mathbf{v}_{e0} \times \mathbf{B}_0$.

Minimum variance analysis has been applied to the magnetic field rotation to obtain the normal direction (\mathbf{N}) of the magnetopause. \mathbf{L} is close to \mathbf{Z} GSE, and \mathbf{M} closes the system ($\mathbf{L} = [0.13, 0.22, 0.97]$, $\mathbf{M} = [0.21, -0.96, 0.19]$, and $\mathbf{N} = [0.97, 0.17, -0.17]$). The magnetic field in LMN coordinates is given in Figure 2a. We concentrate on the \mathbf{N} component of the Ohm's law (equation (1)), i.e., the Hall electric field (E_n) and the terms balancing it (Figure 1b). The \mathbf{N} component of the term $\mathbf{E} + \mathbf{v}_i \times \mathbf{B}$ is plotted in Figure 2b. The parameter v_i is obtained from FPI and \mathbf{B} from FGM. The electric field is obtained in two ways (E_{sdp} and E_{fpi}): measured by the Spin-plane Double Probes (SDP, black) [Lindqvist et al., 2014] and assuming $\mathbf{E} \cdot \mathbf{B} = 0$ (E_{sdp}), and from the electron bulk velocity (\mathbf{v}_e) by assuming $\mathbf{E} = -\mathbf{v}_e \times \mathbf{B}$ (blue), where \mathbf{v}_e is obtained from FPI (E_{fpi}). The two curves do not agree while MMS4 is in the magnetosphere (tenuous plasma with cold ions, shadowed in gray). Our interpretation is that SDP were affected by a cold ion wake [Engwall et al., 2006; Toledo-Redondo et al., 2016]. After 06:05:04.9 UTC, cold ions are heated and magnetosheath ions dominate the mass density, so a cold ion wake is not expected anymore, and $E_{sdp} \approx E_{fpi}$. A layer of large E_n is observed between 06:05:04.25 UTC and 06:05:06.5 UTC (L_1), corresponding to a width of ~ 180 km, i.e., roughly 18 times the cold ion gyroradius ($r_{ci} \approx 10$ km taking $B/\mu_0 = 60$ nT and $T_{ci} \approx 15$ eV). The width of L_1 is inferred from the magnetopause velocity, $v_{MP} \approx -80$ km/s in the \mathbf{N} direction, obtained by timing the \mathbf{B} rotation observed by the four spacecraft [Russell et al., 1983]. The right-hand side terms of equation (1) are plotted in Figure 2c. The current \mathbf{j} is estimated in two ways: directly from FPI on MMS4 by using $\mathbf{j} = en_e(\mathbf{v}_i - \mathbf{v}_e)$ (black) and from the curlometer technique [Dunlop et al., 1988] by using \mathbf{B} field measurements on the four spacecraft ($\mathbf{j} = \nabla \times \mathbf{B} / \mu_0$, blue curve).

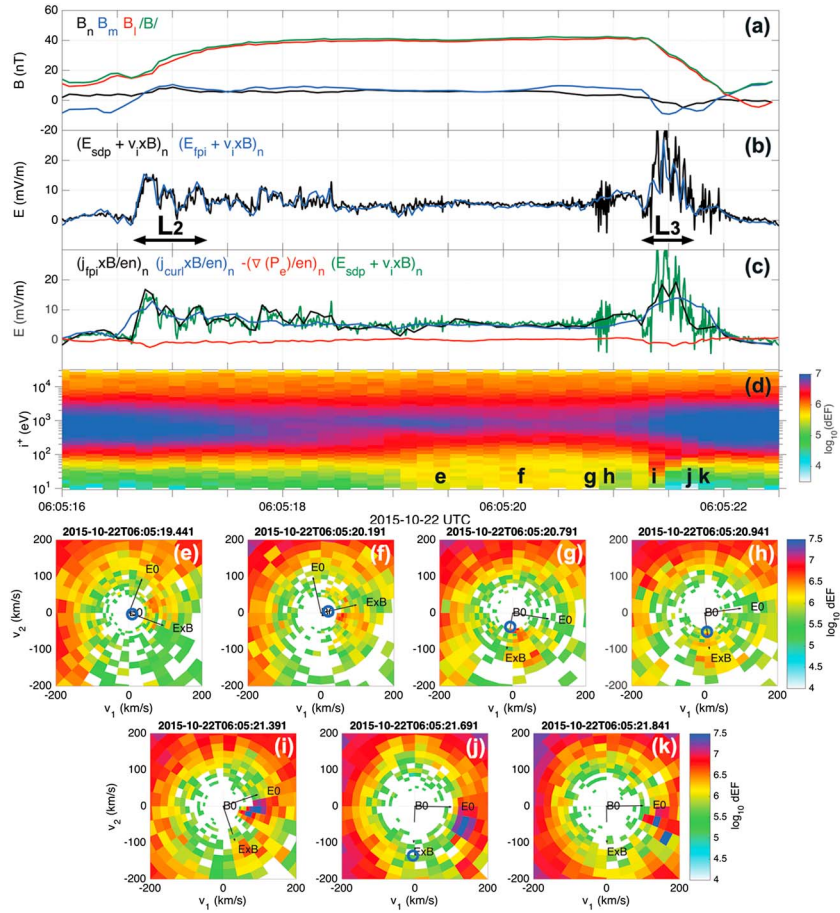


Figure 3. Detail of MMS decoupling region crossing near the X-line. (a) Magnetic field in LMN coordinates. (b) **N** component of the left-hand side terms of equation (1). **E** field is obtained from SDP (E_{sdp} , black) and from electron motion assuming $\mathbf{E} = -\mathbf{v}_e \times \mathbf{B}$ (E_{fpi} , blue). (c) **N** component of the right-hand side terms of equation (1). The current is obtained from FPI (\mathbf{j}_{fpi} , black) and from curlometer (\mathbf{j}_{curl} , blue). The estimation of left-hand side terms (**N** component) of equation (1) is plotted in green for comparison. (d) Ion differential energy flux in $\text{keV cm}^{-2} \text{ s}^{-1} \text{ keV}^{-1}$. (e–k) Projections of ion differential energy flux in the perpendicular plane at different times during the crossing. The parameter v_1 is closest to **N** and v_2 is roughly $-\mathbf{M}$. The electron bulk velocity is plotted using blue circles. \mathbf{B}_0 is the average magnetic field for the FPI interval (150 ms), obtained from FGM. The \mathbf{E}_0 direction is obtained from the average electron bulk velocity in the interval (150 ms) assuming $\mathbf{E}_0 = -\mathbf{v}_{e0} \times \mathbf{B}_0$.

The two estimations of $\mathbf{j} \times \mathbf{B}/en$ agree, although the curlometer technique is not capable of resolving scales below the spacecraft separation (15 km). The density used for the calculation corresponds to n_e . The estimation of $-(\nabla \cdot \mathbf{P}_e)/en$ (red) is always below 2 mV/m, although our calculation cannot resolve variations at length scales below the spacecraft separation (~ 15 km). \mathbf{P}_e corresponds to the electron pressure tensor and it is obtained from FPI moments. The divergence is inferred from the four spacecraft measurements of \mathbf{P}_e , and n_e is used to obtain $-(\nabla \cdot \mathbf{P}_e)/en$. The contribution of $-(\nabla \cdot \mathbf{P}_e)/en$ is small and anticorrelated when compared to the contribution of $\mathbf{j} \times \mathbf{B}/en$, consistent with the findings in *Henderson et al.* [2006]. Figure 2c shows that $\mathbf{E}_{sdp} + \mathbf{v}_i \times \mathbf{B} \approx \mathbf{j} \times \mathbf{B}/en$ outside the region affected by a cold ion wake (green and black curves outside the gray-shadowed region). The Figure 2d (Figure 2e) correspond to the ion (electron) dEF of the interval. The cold ions gain energy in the region of large E_n owing to $\mathbf{E} \times \mathbf{B}$ motion and then mix with the sheath ions. At 06:05:02.5 UTC the electron edge of the separatrix region is crossed (Figure 2e), and the cold ion population is slightly heated (6–8 eV). Figures 2f–2i correspond to differential energy flux for ions in the plane perpendicular to **B**. v_1 is perpendicular to **B** and close to **N** and v_2 closes the system (roughly $-\mathbf{M}$). The electron bulk velocity is indicated using blue circles. The cold ion population remains magnetized together with electrons during the entire separatrix crossing, including inside the region of enhanced E_n (Figure 2i) where hot ions are demagnetized, as indicated by the large $\mathbf{j} \times \mathbf{B}/en$. This cold ion behavior can be observed

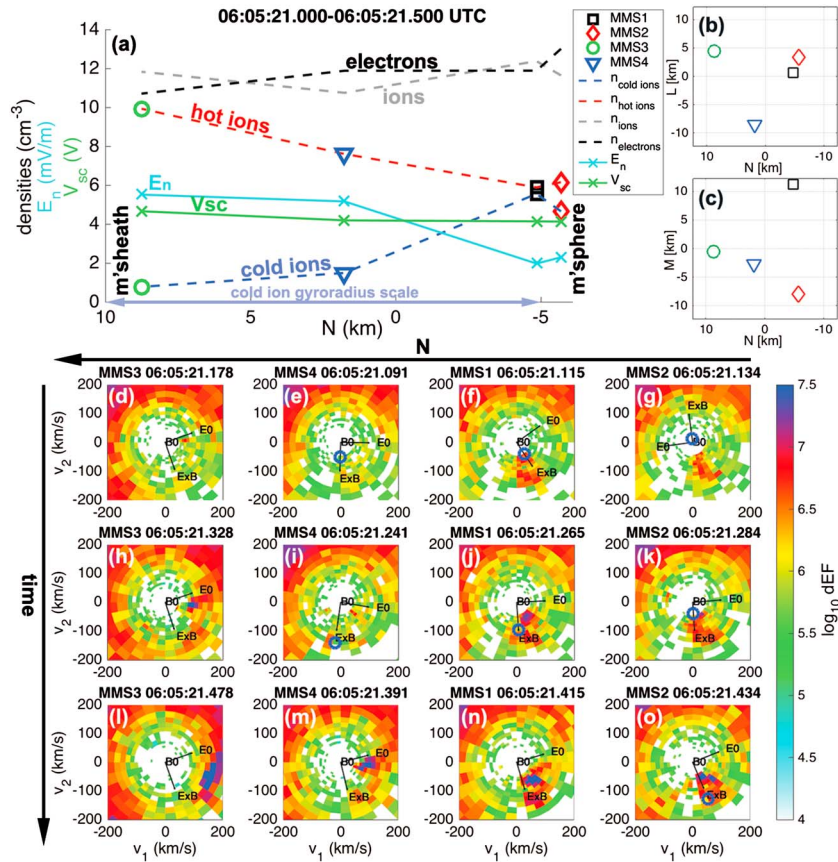


Figure 4. MMS crossing of the cold IDR, 06:05:21.0 UTC–06:05:21.5 UTC. (a) Density of electrons (black), ions (gray), hot ions (red) and cold ions (dark blue), E_n (cyan), and spacecraft potential (V_{sc}) as a function of N position (roughly GSE X). Each MMS spacecraft provides one measurement integrated in the interval 06:05:21.0 UTC–06:05:21.5 UTC. (b, c) Position of the four MMS spacecraft in the NL and NM planes. (d–o) Projections of ion differential energy flux in $\text{keV cm}^{-2} \text{s}^{-1} \text{sr}^{-1} \text{keV}^{-1}$ in the perpendicular plane for the four satellites (columns) and three consecutive times (rows). v_1 is as closest to GSE X and v_2 closes the system. The electron bulk velocity is plotted using blue circles. \mathbf{B}_0 is the average magnetic field for each interval (0.15 s), obtained from FGM. The \mathbf{E}_0 direction is obtained from the average electron bulk velocity in the interval (0.15 s) assuming $\mathbf{E}_0 = -\mathbf{v}_{e0} \times \mathbf{B}_0$.

during the entire interval at all four spacecraft and shows a partial ion demagnetization inside L_1 : hot ions are demagnetized, cold ions and electrons are magnetized.

The N velocity component (inflow velocity) of the cold ions is roughly -65 km/s in the spacecraft frame, i.e., $+15 \text{ km/s}$ in the magnetopause frame ($v_{MP} \simeq -80 \text{ km/s}$), corresponding roughly to 0.1 times the jet velocity. Measuring a finite inflow velocity confirms that reconnection is ongoing.

Figure 3 corresponds to the interval when MMS was close to the X-line ($\sim 06:05:16 \text{ UTC} - 06:05:22 \text{ UTC}$), since it observes a jet reversal (see Figure 1) and the magnetopause motion is determined to be small, $|v_{MP}| < 30 \text{ km/s}$. The \mathbf{B} field in LMN coordinates is shown in Figure 3a, and it mainly corresponds to the magnetospheric \mathbf{B} . B_m shows a signature at $\sim 06:05:21.5 \text{ UTC}$ consistent with the bipolar Hall \mathbf{B} field. The left-hand side term of equation (1) is presented in Figure 3b. The electric field is obtained from SDP (black) and FPI (blue), in the same way as for Figure 2b. Their agreement indicates that electrons are magnetized and follow $\mathbf{E} \times \mathbf{B}$ motion. In Figure 3c the right-hand side terms of equation (1) are shown, i.e., $\mathbf{j} \times \mathbf{B}/en$ (blue, black) and $-(\nabla \cdot \mathbf{P}_e)/en$ (red), and compared to $\mathbf{E}_{sdp} + \mathbf{v}_i \times \mathbf{B}$ (green). The parameter \mathbf{j} is obtained from FPI (black) and curlometer (blue), see comments to Figure 2c. The $-(\nabla \cdot \mathbf{P}_e)/en$ term is less than 2 mV/m in our calculation from four spacecraft, and its contribution to the electric field is anticorrelated with the Hall term (see comments to Figure 2).

During the interval 06:05:18 UTC–06:05:21 UTC, $\mathbf{j} \times \mathbf{B}/en$ term is larger than 5 mV/m, hot ions are demagnetized while cold ions and electrons remain magnetized (Figures 3e–3h), so we conclude that MMS4 is inside a

hot IDR. Two layers (L_2, L_3) of large E_n are crossed: at 06:05:16.75 UTC and 06:05:21.5 UTC. Inside L_2 FPI did not detect cold ions (Figure 3d), and therefore, we concentrate on L_3 . Its length scale, $L_3 \simeq 15$ km ($v_{MP} \simeq 30$ km/s), is smaller than for the previous separatrix crossing reported in Figure 2 ($L_1 \simeq 180$ km). The size of L_3 is on the order of the cold ion gyroradius ($L_3 \simeq r_{ci} = 15$ km, taking $|B| = 40$ nT and $T_{ci} = 20$ eV). Inside the layer at 06:05:21.4 UTC, cold ions stop following the $\mathbf{E} \times \mathbf{B}$ motion and are accelerated parallel to \mathbf{E} (Figures 3i–3k). The interface between the hot IDR and the cold IDR (L_3) occurs at 06:05:21.35 UT (large increase of the \mathbf{E} field measured by SDP), consistent with Figure 3i (FPI measurement in the interval 06:05:21.316 UT–06:05:21.466 UT) where a mixture of $\mathbf{E} \times \mathbf{B}$ drifting cold ions and accelerated parallel to \mathbf{E} cold ions is observed. The same cold ion behavior is observed by MMS1–3 inside the large E_n layer (L_3), where only electrons remain magnetized and follow $\mathbf{E} \times \mathbf{B}$.

Inside L_3 , the \mathbf{E} field becomes large, so the cold ion population has larger energy and can be detected by FPI. The spacecraft separation was on the order of the cold ion gyroradius, so this length scale can be resolved. We present detailed plots of the interval 06:05:21.0 UTC–06:05:21.5 UTC for the four spacecraft in Figure 4. The electron (dashed black) and ion (dashed gray) number densities as a function of N , shown in Figure 4a, are roughly in agreement, indicating that there is no large hidden cold ion population during that interval. The hot ion (above 100 eV) number density is obtained from a partial moment calculation and plotted in red. The cold ion density (dark blue) corresponds to a partial moments calculation considering energies below 100 eV, and only a portion of the sky map, to avoid contamination from magnetosheath ions (see Figure S1 in the supporting information for a detailed description). A large cold ion density gradient ($4\text{--}5$ cm $^{-3}$ in 10–15 km) is observed between MMS3–4 (inside L_3) and MMS1–2 (outside L_3). Figures 4b–4c show the relative positions in the \mathbf{NL} and \mathbf{NM} planes. Finally, we calculate the ion distributions (dEF) in the perpendicular velocity plane for the four spacecraft (columns) and for the three FPI data points inside the interval (rows), Figures 4d–4o. MMS1–2, i.e., Figures 4f, 4g, 4j, 4k, 4n, and 4o, observe magnetized cold ions outside L_3 , except in Figure 4g where the average $\mathbf{E} \times \mathbf{B}$ velocity is close to zero (blue circle) and therefore the obtained $\mathbf{E} \times \mathbf{B}$ direction is not reliable. On the other hand, MMS3–4, i.e., Figures 4d, 4e, 4h, 4i, 4l, and 4m, are inside L_3 (see E_n in Figure 4a) and observe cold ions accelerated parallel to \mathbf{E} . These are the first observations, to our knowledge, of cold ion demagnetization inside a structure below the cold ion length scale.

The Hot Plasma Composition Analyzer (HPCA) [Young *et al.*, 2014] onboard MMS resolves the different masses of the ion populations in the energy range ~ 1 eV–40 keV and covers the full sky every 10 s. HPCA (MMS4) measured a cold (i.e., below 100 eV) He $^+$ number density of ~ 0.35 cm $^{-3}$ during the interval 06:04:32 UTC–06:05:02 UTC (i.e., the magnetospheric side of crossing 1, see Figure S2 in the supporting information). HPCA on MMS1–3 measured similar quantities. From Figure 1e we estimate that the total number density in the magnetosphere is ~ 5 cm $^{-3}$, so He $^+$ represents $\sim 23\%$ of the ion mass density.

4. Discussion and Conclusion

During the interval studied, MMS crossed three narrow layers of large E_n (L_1 – L_3). Inside L_2 there are few cold ion counts and we cannot determine their behavior. L_2 apparently was near the magnetosheath side where cold ions may be less abundant. L_1 is located far from the X-line and corresponds to a layer of size $L_1 \simeq 180$ km, much larger than the magnetospheric cold ion population gyroradius ($r_{ci} \simeq 10$ km). The cold ions remain magnetized inside the region together with electrons, as opposed to hot ions which are demagnetized, reducing the Hall currents carried by electrons and being responsible for part of the \mathbf{E} field balance via $-\mathbf{v}_i \times \mathbf{B}$ [Toledo-Redondo *et al.*, 2015]. On the other hand, L_3 is located close to the X-line between a jet reversal, and $L_3 \simeq 15$ km, similar to the cold ion gyroradius. Inside L_3 we directly observe cold ions accelerating parallel to \mathbf{E} , and therefore only electrons remain magnetized inside this narrow layer. Between the L_2 and L_3 crossings MMS was in a region where hot ions are demagnetized and cold ions magnetized (hot IDR). We cannot determine its size because MMS did not entirely cross the layer. The E_n field in this intermediate region was less than half of the E_n field of the cold IDR (L_3). A sharp (~ 0.5 cm $^{-3}$ km $^{-1}$) cold ion density gradient separates the two regions, suggesting that cold ions are rapidly heated inside the cold IDR.

The measurements indicate that $\sim 23\%$ of the ion mass density correspond to He $^+$, consistent with the findings in Fuselier *et al.* [2016]. The gyroradius of H $^+$ and He $^+$ differ by a factor of 2 so He $^+$ is expected to demagnetize at larger scales. This effect should be more evident for a cold ion population with significant O $^+$ [Markidis *et al.*, 2011].

Magnetic reconnection generates large **E** fields and waves that heat the cold ions, modifying their gyroradius length scale [Toledo-Redondo et al., 2016]. The cold ion heating modifies the microphysics arising at the cold ion length scale and eventually both processes may reach an equilibrium situation. Future simulations including cold ions will help us in understanding the large-scale implications of multiple ion temperatures on magnetic reconnection and the interrelation between heating and the new microphysics.

We reported, for the first time, observations of a subregion (cold IDR) of the size of the cold ion gyroradius embedded inside the (hot) IDR. We conclude that a multilayered IDR must be considered when different temperature ion populations are present in magnetic reconnection. The associated currents, electric fields, and ion-heating mechanisms differ on each region. In closing, we note that multiple ion temperatures should be a common scenario in many astrophysical plasmas.

Acknowledgments

We would like to congratulate all the people involved in the MMS project for all their efforts during this early stage of the mission and the high quality achieved that will provide us great scientific return. S.T.R. holds an ESA Fellowship and acknowledges support from the science faculty of the European Space Astronomy Centre (ESAC). MMS data are available to the public in the MMS Science Data Center (<https://lasp.colorado.edu/mms/sdc/public/>).

References

- André, M., and C. M. Cully (2012), Low-energy ions: A previously hidden solar system particle population, *Geophys. Res. Lett.*, *39*, L03101, doi:10.1029/2011GL050242.
- André, M., A. Vaivads, Y. V. Khotyaintsev, T. Laitinen, H. Nilsson, G. Stenberg, A. Fazakerley, and J. Trotignon (2010), Magnetic reconnection and cold plasma at the magnetopause, *Geophys. Res. Lett.*, *37*, L22108, doi:10.1029/2010GL044611.
- Borovsky, J. E., M. Hesse, J. Birn, and M. M. Kuznetsova (2008), What determines the reconnection rate at the dayside magnetosphere?, *J. Geophys. Res.*, *113*, A07210, doi:10.1029/2007JA012645.
- Burch, J. L., T. E. Moore, R. B. Torbert, and B. L. Giles (2015), Magnetospheric multiscale overview and science objectives, *Space Sci. Rev.*, *199*(1–4), 5–21.
- Burch, J. L., et al. (2016), Electron-scale measurements of magnetic reconnection in space, *Science*, *352*, aaf2939, doi:10.1126/science.aaf2939.
- Cassak, P., and M. Shay (2007), Scaling of asymmetric magnetic reconnection: General theory and collisional simulations, *Phys. Plasmas*, *14*(10), 102114, doi:10.1063/1.2795630.
- Chandler, M. O., S. A. Fuselier, M. Lockwood, and T. E. Moore (1999), Evidence of component merging equatorward of the cusp, *J. Geophys. Res.*, *104*(A10), 22,623–22,633, doi:10.1029/1999JA900175.
- Chandler, M. O., and T. E. Moore (2003), Observations of the geopause at the equatorial magnetopause: Density and temperature, *Geophys. Res. Lett.*, *30*(1869), doi:10.1029/2003GL017611.
- Chappell, C. R., M. M. Huddleston, T. E. Moore, B. L. Giles, and D. C. Delcourt (2008), Observations of the warm plasma cloak and an explanation of its formation in the magnetosphere, *J. Geophys. Res.*, *113*, A09206, doi:10.1029/2007JA012945.
- Chen, S.-H., and T. E. Moore (2004), Dayside flow bursts in the Earth's outer magnetosphere, *J. Geophys. Res.*, *109*, A03215, doi:10.1029/2003JA010007.
- Chen, S.-H., and T. E. Moore (2006), Magnetospheric convection and thermal ions in the dayside outer magnetosphere, *J. Geophys. Res.*, *111*, A03215, doi:10.1029/2005JA011084.
- Darrrouzet, F., J. D. Keyser, P. Décréau, F. E. Lemdani-Mazouz, and X. Vallières (2008), Statistical analysis of plasmaspheric plumes with Cluster/WHISPER observations, *Ann. Geophys.*, *26*, 2403–2417.
- Darrrouzet, F., et al. (2009), Plasmaspheric density structures and dynamics: Properties observed by the CLUSTER and IMAGE missions, in *The Earth's Plasmasphere*, pp. 55–106, Springer, New York.
- Dunlop, M., D. Southwood, K.-H. Glassmeier, and F. Neubauer (1988), Analysis of multipoint magnetometer data, *Adv. Space Res.*, *8*(9–10), 273–277.
- Engwall, E., A. I. Eriksson, and J. Forest (2006), Wake formation behind positively charged spacecraft in flowing tenuous plasmas, *Phys. Plasmas*, *13*(6), 62904.
- Fuselier, S. A., et al. (2016), Magnetospheric ion influence on magnetic reconnection at the duskside magnetopause, *Geophys. Res. Lett.*, *43*, 1435–1442, doi:10.1002/2015GL067358.
- Henderson, P. D., C. J. Owen, A. D. Lahiff, I. V. Alexeev, A. N. Fazakerley, E. Lucek, and H. Rème (2006), Cluster peace observations of electron pressure tensor divergence in the magnetotail, *Geophys. Res. Lett.*, *33*, L22106, doi:10.1029/2006GL027868.
- Lavraud, B., et al. (2016), Currents and associated electron scattering and bouncing near the diffusion region at Earth's magnetopause, *Geophys. Res. Lett.*, *43*, 3042–3050, doi:10.1002/2016GL068359.
- Lee, S. H., H. Zhang, Q.-G. Zong, A. Otto, H. Rème, and E. Liebert (2016), A statistical study of plasmaspheric plumes and ionospheric outflows observed at the dayside magnetopause, *J. Geophys. Res. Space Physics*, *121*, 492–506, doi:10.1002/2015JA021540.
- Lindqvist, P.-A., et al. (2014), The spin-plane double probe electric field instrument for MMS, *Space Sci. Rev.*, *199*, 137–165, doi:10.1007/s11214-014-0116-9.
- Markidis, S., G. Lapenta, L. Bettarini, M. Goldman, D. Newman, and L. Andersson (2011), Kinetic simulations of magnetic reconnection in presence of a background O⁺ population, *J. Geophys. Res.*, *116*, A00K16, doi:10.1029/2011JA016429.
- Pollock, C. J., et al. (2016), Fast plasma investigation for magnetospheric multiscale, *Space Sci. Rev.*, *199*, 331–406, doi:10.1007/s11214-016-0245-4.
- Pritchett, P. (2008), Collisionless magnetic reconnection in an asymmetric current sheet, *J. Geophys. Res.*, *113*, A06210, doi:10.1029/2007JA012930.
- Pritchett, P., and F. S. Mozer (2009), Asymmetric magnetic reconnection in the presence of a guide field, *J. Geophys. Res.*, *114*, A11210, doi:10.1029/2009JA014343.
- Russell, C., J. Gosling, R. Zwickl, and E. Smith (1983), Multiple spacecraft observations of interplanetary shocks: ISEE three-dimensional plasma measurements, *J. Geophys. Res.*, *88*(A12), 9941–9947.
- Russell, C., et al. (2016), The magnetospheric multiscale magnetometers, *Space Sci. Rev.*, *199*(1), 189–256.
- Sauvaud, J.-A., et al. (2001), Intermittent thermal plasma acceleration linked to sporadic motions of the magnetopause, first Cluster results, *Ann. Geophys.*, *19*, 1523–1532.
- Toledo-Redondo, S., A. Vaivads, M. André, and Y. V. Khotyaintsev (2015), Modification of the Hall physics in magnetic reconnection due to cold ions at the Earth's magnetopause, *Geophys. Res. Lett.*, *42*, 6146–6154, doi:10.1002/2015GL065129.

- Toledo-Redondo, S., M. André, A. Vaivads, Y. V. Khotyaintsev, B. Lavraud, D. Graham, A. Divin, and N. Aunai (2016), Cold ion heating at the dayside magnetopause during magnetic reconnection, *Geophys. Res. Lett.*, *43*, 58–66, doi:10.1002/2015GL067187.
- Walsh, B., D. Sibeck, Y. Nishimura, and V. Angelopoulos (2013), Statistical analysis of the plasmaspheric plume at the magnetopause, *J. Geophys. Res. Space Physics*, *118*, 4844–4851, doi:10.1002/jgra.50458.
- Walsh, B., T. Phan, D. Sibeck, and V. Souza (2014), The plasmaspheric plume and magnetopause reconnection, *Geophys. Res. Lett.*, *41*, 223–228, doi:10.1002/2013GL058802.
- Wang, S., L. M. Kistler, C. G. Mouikis, and S. M. Petrinec (2015), Dependence of the dayside magnetopause reconnection rate on local conditions, *J. Geophys. Res. Space Physics*, *120*, 6386–6408, doi:10.1002/2015JA021524.
- Young, D. T., et al. (2014), Hot plasma composition analyzer for the magnetospheric multiscale mission, *Space Sci. Rev.*, *199*, 407–470, doi:10.1007/s11214-014-0119-6.